Carbon Letters (2019) 29:289–296
https://doi.org/10.1007/s42823-019-00025-z

Online ISSN 2233-4998
Print ISSN 1976-4251

ORIGINAL ARTICLE

Nitrogen-doped nanoporous carbons derived from lignin for high CO_2 capacity

Sohyun Park[1] · Min Sung Choi[1] · Ho Seok Park[1]

Received: 21 August 2018 / Accepted: 20 September 2018 / Published online: 29 January 2019

Abstract
In this paper, nitrogen (*N*)-doped ultra-porous carbon derived from lignin is synthesized through hydrothermal carbonization, KOH activation, and post-doping process for CO_2 adsorption. The specific surface areas of obtained *N*-doped porous carbons range from 247 to 3064 m^2/g due to a successful KOH activation. *N*-containing groups of 0.62–1.17 wt% including pyridinic *N*, pyridone *N*, pyridine-*N*-oxide are found on the surface of porous carbon. *N*-doped porous carbon achieves the maximum CO_2 adsorption capacity of 13.6 mmol/g at 25 °C up to 10 atm and high stability over 10 adsorption/desorption cycles. As confirmed by enthalpy calculation with the Clausius–Clapeyron equation, an adsorption heat of *N*-doped porous carbon is higher than non-doped porous carbon, indicating a role of *N* functionalities for enhanced CO_2 adsorption capability. The overall results suggest that this carbon has high CO_2 capture capacity and can be easily regenerated and reused without any clear loss of CO_2 adsorption capacity.

Keywords Porous carbon · Microporous · Biomass · Lignin · Chemical activation · Nitrogen doping · CO_2 capture

1 Introduction

Recent concerns about climate change and global warming arising from the emission of greenhouse gases are rapidly increasing [1]. In particular, CO_2 takes up a substantial portion among the greenhouse gases: a total amount of CO_2 emitted in a year is about 33 Gt and its concentration is over 400 ppm in atmosphere [2]. Therefore, CO_2 capture is considered a critical technology to resolve these issues and, particularly, adsorption has been extensively investigated due to high repeatability and selectivity [3]. Adsorbents, including porous carbons [4], zeolites [5], metal–organic framework (MOF) [6], and graphenes [7] are the key to determine adsorption performances. Among the proposed adsorption materials, porous carbons have received significant attention because they have certain benefits like cost effectiveness, easy handling, and chemical, mechanical, and thermal stabilities [3, 8]. In particular, the surface and porous structures of porous carbons can be controlled by varying the synthetic conditions and the types of precursors, which indicates the potential of improving the adsorption performance [9].

The interaction of porous carbons with CO_2 on the large pore surface is a deterministic parameter of the adsorption feature, the so-called isotherm. Thus, nitrogen (*N*) incorporation onto the porous carbons is promising due to a high adsorption capacity and hydrophobicity, which results in enhancing CO_2 adsorption capabilities via acid–base interaction [1], quadrupolar interaction [10], and/or hydrogen bonding interactions [11]. *N*-containing groups increase the surface basicity of carbon materials by means of an electron-donating ability, resulting in a more favorable interaction with acidic CO_2 [12]. This chemical effect of *N*-doped carbons on the CO_2 uptake depends on the identities of bonding configurations in the forms of pyrrole/pyridone, pyridinic, and pyridine-*N*-oxide along with the pore size and interconnectivity of the adsorbent [13].

Another consideration for the design of porous carbons is the types of precursors. Recently, wood biomass resources have been used as promising precursors to replace fossil fuel-based ones, because they are abundant, sustainable and cost-effective [14]. Examples of wood biomasses, which are

Electronic supplementary material The online version of this article (https://doi.org/10.1007/s42823-019-00025-z) contains supplementary material, which is available to authorized users.

✉ Ho Seok Park
phs0727@skku.edu

[1] School of Chemical Engineering, College of Engineering, Sungkyunkwan University, 2066 Seobu-ro, Jangan-gu, Suwon, Gyeonggi-do 440-746, Republic of Korea

composed of cellulose, lignin and hemicellulose, include rice straw [15], coconut shell [16], beer waste [17], macadamia nut shell [18] and pine cone [19]. Lignin, the second most abundant organic material in nature, is thought to be a good precursor of porous carbon owing to low cost, natural abundance, and industrial-scale production as a byproduct of wood industries [20]. In this work, we used lignosulfonate acid sodium salt as a carbon precursor to systematically study the effect of porous structure and *N* groups on the CO_2 adsorption performances. The post-treatment with urea was carried out to introduce *N* functionality onto the porous carbon surface, as well as to further increase the surface area by additional activation.

2 Experimental section

2.1 Synthesis of hydrothermal lignin (HyL)

Hydrothermal lignin (HyL) is prepared from lignin product, lignosulfonate acid sodium salt through hydrothermal carbonization process. 1 g of lignin product was soaked in 10 g of deionized (DI) water and stirred for a while. After stirring, the soaked lignin was put into a 20 ml autoclave reactor and heated up to 200 °C for 12 h. After the carbonization step, carbon materials were washed with DI water and dried in freeze dryer for 72 h. The obtained carbon structure is notated as HyL.

2.2 Synthesis of KOH-activated HyL (KL700)

In order to fabricate a microporous carbon structure from the obtained HyL, chemical activation using KOH as an activation agent was empolyed. In a typical preparation process, 0.4 g of HyL and 1.2 g potassium hydroxide were uniformly mixed in mortar. Afterward, the samples were activated to 700 °C for 2 h under argon atmosphere. During the activation process, the heating rate was 5 °C/min, and the argon flow rate was 100 cc/min. After the activation, all the products were rinsed with diluted HCl to eliminate K^+ ion. After washing with HCl, the wet products were washed with DI water until the pH value was 7. And, the products were dried in a freeze dryer for 72 h. The obtained porous carbon is named as KL700.

2.3 Synthesis of *N*-doped KL700, *x*N-KL

For synthesis of *N*-doped carbon sample, urea [$(NH_2)_2CO$] was used as nitrogen precursor. In a typical synthesis, 200 mg of urea and 50 mg of KL700 were mixed in 30 ml DI water with vigorous stirring. The obtained solution was dried in a vacuum evaporator in 50 °C water bath. Then, the product was pyrolyzed at 800 °C 1 h under an argon atmosphere. During the pyrolysis, the heating rate was 5 °C/min, and the argon flow rate was 100 cc/min. The obtained specimen is denoted as 4 N-KL. For comparison, the amount of urea was changed to 50, 100, 200, 400 mg, while the amount of KL700 was fixed as 50 mg. After that, obtained materials are denoted as *x*N-KL, and the *x* of the *x*N-KL means the mass ratio of the urea versus KL700.

2.4 Materials' characterizations

Scanning electron microscopy (SEM) images were obtained on a FE-SEM (LEO SUPRA 55) and transmission electron microscopy (TEM) images were obtained using a Libra 200 HT Mc Cs, 200 kV. N_2 adsorption/desorption isotherms were obtained by a Brunauer–Emmett–Teller apparatus (BET, BELSORP-mini II). Before measurement, the samples were prepared under vacuum condition at 200 °C for 12 h. The Brunauer–Emmett–Teller (BET) method was used to calculate the specific surface area (SSA) of the samples. The pore-size distributions were derived by the Barrett–Joyner–Halenda (BJH) model. Raman spectra and X-ray photoelectron spectroscopy (XPS) were prepared to determine the chemical structures and compositions of the samples. Raman spectroscopy was conducted using a SENTERRA Raman microscope (Bruker) with a 532 nm laser. XPS data were obtained using a monochromatic Al-Ka (AXIS-NOVA and Ultra DLD, 1486.6 eV). CO_2 adsorption data was measured by a high-pressure gas adsorption analyzer (BELSORP-HP, BEL Japan).

2.5 CO_2 adsorption measurement

Before checking the adsorption data, all adsorbents underwent the pre-treatment step at 200 °C in vacuum. The amount of *N*-doped carbon which was used for the adsorption experiment is at least 50 mg. CO_2 adsorption measurement with different adsorbents was implemented at 25 °C. For the adsorption enthalpy calculation, CO_2 adsorption was implemented at different temperatures, 25 °C and 50 °C. To measure the cyclability of adsorption and desorption, ten continuous cycle of CO_2 adsorption–desorption were performed from 0.05 to 10 atm with the same instrument, BELSORP-HP.

3 Results and discussion

3.1 Materials' characteristics

The surface morphology of the samples was investigated by SEM and TEM measurement. As shown in the SEM image (Fig. S1a–c), raw lignin and HyL showed a smooth surface. Comparing Fig. S1a–c, it is clear that the hydrothermal process

made a smaller particle than raw lignin which was a macroparticle. While undergoing hydrothermal carbonization, the lignin product successfully went through the carbonization step which converted biomass into a carbon-densified product at high yield [21]. And, its weak parts and impurities easily underwent degradation to form small molecules though hydrolysis, dehydration and decarboxylation [22]. And, these weak functional groups became small defect molecules which were dissolved in the solution. Because of the small particle size, hydrothermal lignin has a large specific surface area by itself. From that, it can be driven to ultrahigh surface porous carbon thorough chemical activation. After the KOH activation process, a highly developed porous structure with macro-sized pores and nano-sized pores with a diameter less than 100 nm can be shown (Fig. 1a, b). During the KOH activation, KOH dehydrates to transform to K_2O and H_2O at 400 °C. After that, carbon reacts with H_2O and produces CO and H_2 gas. CO and H_2O react again to make CO_2 and H_2. With CO_2 and K_2O, K_2CO_3 can be formed by following Eq. (1).

$$CO_2 + K_2O \rightarrow K_2CO_3 \quad (1)$$

Around 600 °C, KOH is completely consumed, and K_2CO_3 starts to decompose to CO_2 and K_2O [Eq. (2)].

$$K_2CO_3 \rightarrow K_2O + CO_2 \quad (2)$$

Moreover, CO_2 can react with carbon to make CO at a higher temperature. Also, intercalated K_2CO_3 and K_2O react directly with carbon and oxidize carbon to CO [23]. From these reactions, it is seen that etching was done on the carbon framework by the redox reaction with potassium hydroxide as chemical activating reagent [24]. The etching done on the carbon frame work produced nano-sized pores, and modified the carbon surface uniformly. In a low magnification SEM image of KL700 (Fig. 1a), completely modified surface with various pores through KOH activation can be seen. Except the macro-sized pore whose size is about 10 μm, the other side's surface was modified smoothly after the activation. High magnification SEM image and TEM image of KL700 (Fig. 1b, c) show a nano-sized pore on the surface of KL700 below 10 nm. From high magnification SEM images and TEM image of 4 N-KL, after the post-doping process on

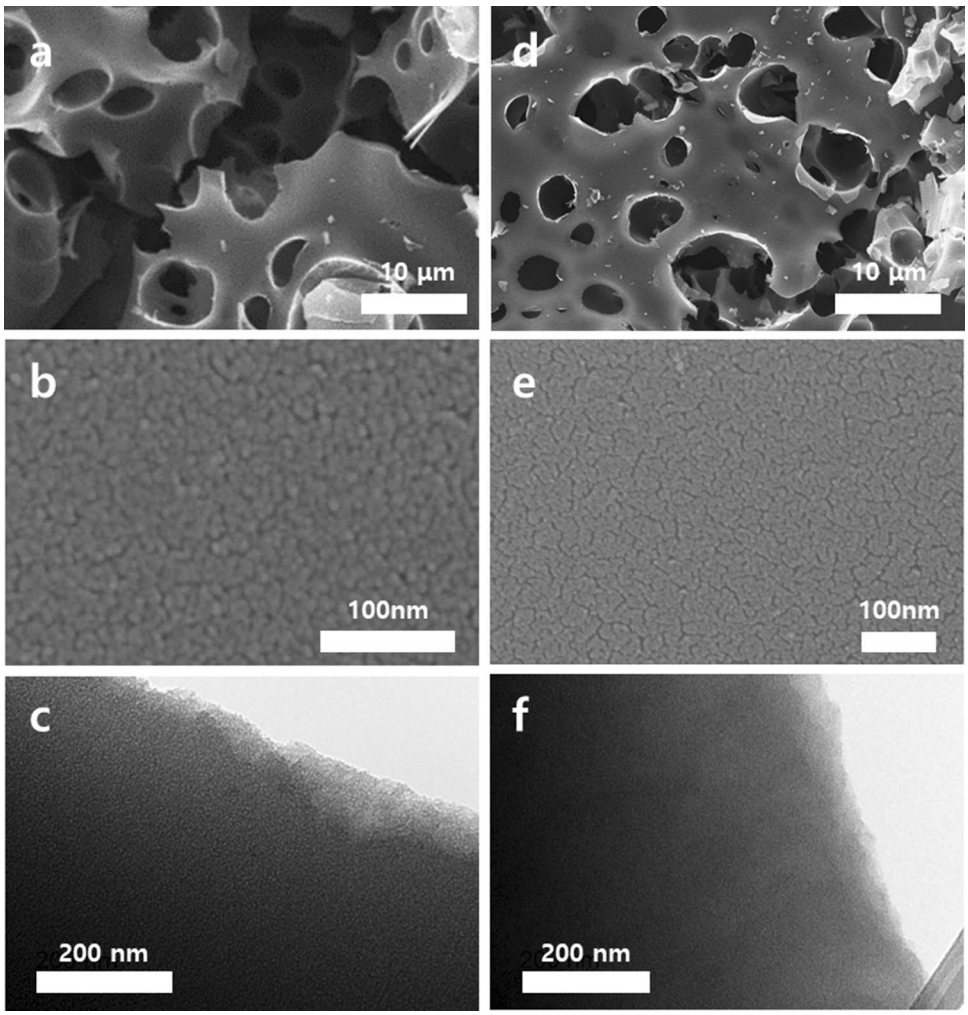

Fig. 1 **a**, **b** SEM images of KL700, **c** TEM image of KL700, **d**, **e** SEM images of 4 N-KL, **f** TEM image of 4 N-KL

KL700, the structure was maintained well, and the nano-sized pores were also maintained uniformly.

The textural properties of the porous carbons are listed in Table 1. It can be seen that the BET surface area and the pore volume increased significantly from 125 to 3170 m^2/g and 1.33 to 1.6 cm^3/g, after KOH activation from HyL. And, after post-doping, of 1 N-KL, 2 N-KL, and 4 N-KL show similar high BET SSA of 3020, 3064, and 3021 m^2/g. SSA of 8 N-KL where eight times more *N* precursor was used than porous carbon decreased to 3170–2470 m^2/g, because the high amount of urea blocked the nano-sized pores. Also, the total pore volume ($V_{tot\ pore}$) of 8 N-KL was 1.26 cm^3/g, which was the lowest among the synthesized porous carbon.

As shown in Fig. 2, the types of adsorption can be classified from the result of N_2-sorption isotherm of HyL (a), KL700 (c), 4 N-KL (e), respectively. From Fig. 2a, HyL showed a type-III isotherm [25, 26]. From Fig. 2b, BJH plot of HyL shows that there is no pore below 10 nm. And, the macro-sized pore whose size is over than 100 nm is dominant. Also, the mean pore dimeter of HyL was measured to be 42.50 nm from Table 1. The isotherm plots in Fig. 2c and e corresponded to type-I curves with well-defined plateaus [27], showing a microporous nature of the KL700, and 4 N-KL [28]. After activation and post-doping, the mean pore diameter was measured around 2 nm which can support that the nano-sized pore was well-developed on the

Table 1 Physical and chemical characteristics of various samples

Samples	Physical properties			Chemical properties		
	SSA (m^2/g)	Mean pore diameter (nm)	$V_{tot\ pore}$ (cm^3/g)	N (wt%)	O (wt%)	C (wt%)
HyL	125	42.50	1.33	–	31.16	68.84
KL700	3172	2.02	1.60	–	12.28	87.72
1 N-KL	3020	2.51	1.89	0.62	19.34	80.03
2 N-KL	3064	2.04	1.56	0.64	12.26	87.10
4 N-KL	3021	2.09	1.58	1.10	9.35	89.55
8 N-KL	2473	2.04	1.26	1.17	11.02	87.81

SSA specific surface area calculated by BET equation, $V_{tot\ pore}$ total pore volume estimated from the adsorption amount of N_2 at $P/P_o = 0.99$

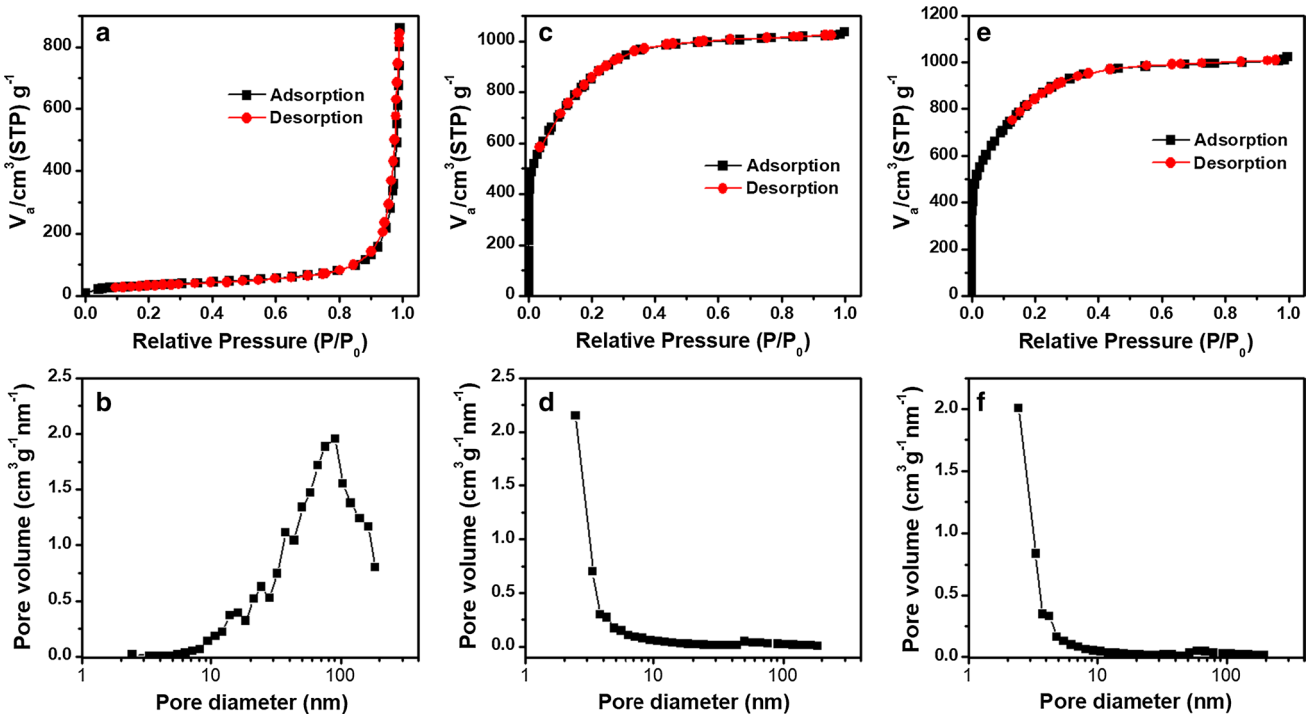

Fig. 2 BET analysis of HyL, KL700, 4 N-KL. N_2 adsorption/desorption isotherm **a** HyL, **c** KL700, **e** 4 N-KL, pore distribution graph **b** HyL, **d** KL700, **f** 4 N-KL

surface of porous carbon, and also after the doping process. Pore-size distribution plots of KL700 and 4 N-KL supported the existence of nano-sized pores below 5 nm (Fig. 2d, f). And, the microporous surface areas (S_{micro}) of KL700 and 4 N-KL calculated using the *t* plot were 3085 and 2943 m^2/g, respectively. These results indicate that KL700 and 4 N-KL contained a microporous structure.

The structures of HyL, KL700, and 4 N-KL were further investigated by Raman spectroscopy as shown in Fig. 3. The D band derived from defective carbon materials can be seen to be around 1330 cm^{-1}, whereas G band which is the result of in-plane vibrations of sp^2-bonded carbon can be seen to be around 1590 cm^{-1}. The D band for HyL is detected at 1330 cm^{-1} and G band is detected at 1565 cm^{-1}, and D band for KL700 can be seen at 1330 cm^{-1} and G band for KL700 at 1575 cm^{-1}. Because of nitrogen doping, the site of D and G band for 4 N-KL slightly changed, D band was at 1335 cm^{-1} and G band at 1580 cm^{-1}. I_D/I_G ratio is related to sp^3/sp^2 carbon ratio which can explain the amount of defect [29]. Therefore, if I_D/I_G ratio is higher than the pristine material, it means that there are more defects on the materials than the pristine material [30]. I_D/I_G ratio for HyL is 0.83, and after the KOH activation, I_D/I_G ratio for KL700 is 0.93 indicating that the KOH activation produced more defect sites with the effect of activation, i.e., etching. The I_D/I_G ratio of 4 N-KL is 0.91 which is almost similar to the ratio of KL700.

Surface chemical component and atomic percentage of the surface elements of HyL, KL700, 4 N-KL samples were evaluated by XPS analysis. From wide XPS spectra (Fig. 4a, Table 1), much of oxygen-containing group was decreased after the activation treatment [24]. Lots of oxygen species in HyL were etched out during the KOH activation, so after the activation, carbon contents increased to 68.84–87.72 wt%. The high-resolution C1 s spectra of HyL (Fig. S2a), KL700 (Fig. S2b) and 4 N-KL (Fig. S2c) can be explained into five individual component peaks, corresponding to C–C (284.6 eV), C=C (284.8 eV), C–O (285.9 eV), C=O (287.5 eV), and O–C=O (289.2 eV), respectively [31]. In KL700, the peak intensity of C=O group dramatically dropped after the activation because of KOH reduction [32]. Besides, nitrogen bonding configurations of 4 N-KL are further characterized by the high-resolution N1s spectra (Fig. 4b). The peaks of N1s spectra

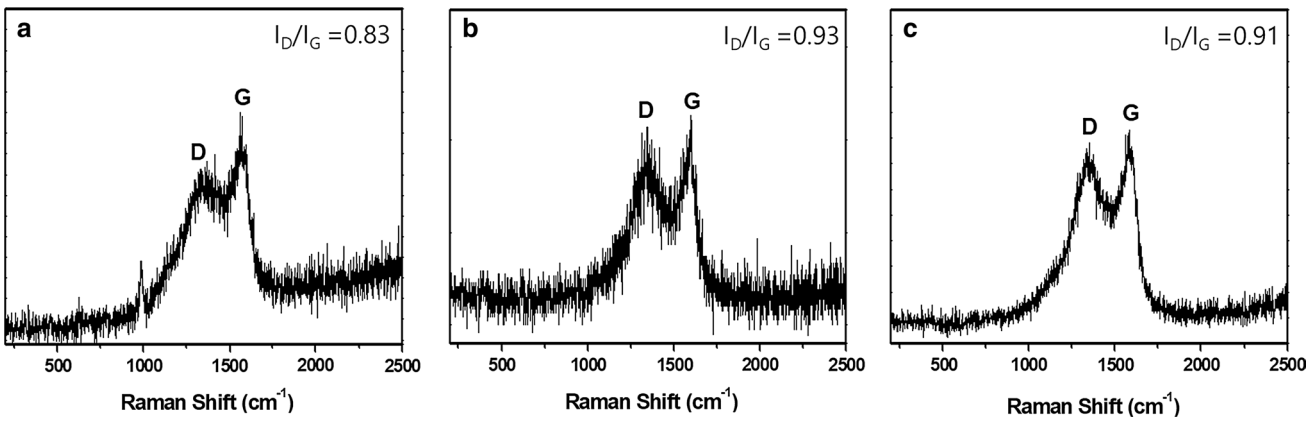

Fig. 3 Raman spectroscopy of **a** HyL, **b** KL700, **c** 4 N-KL

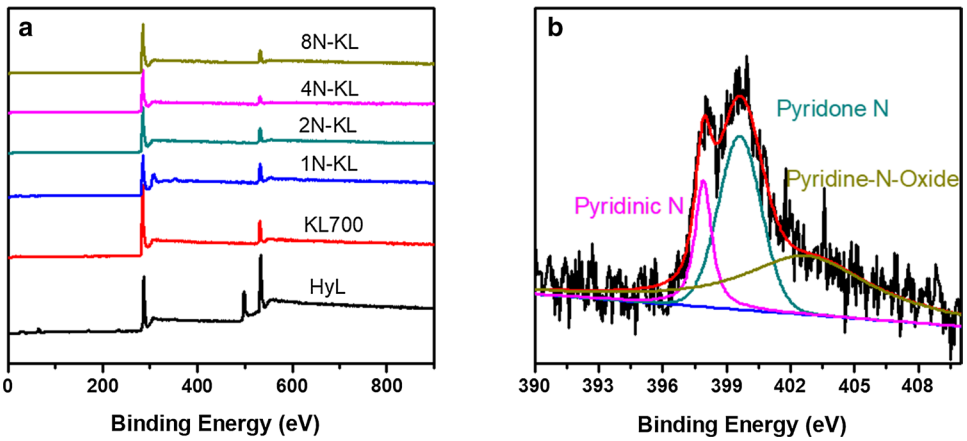

Fig. 4 **a** Wide XPS spectra of HyL, KL700, 1 N-KL to 8 N-KL, **b** N1s peak of 4 N-KL

can be assigned to various *N*-containing groups, including pyridinic *N* (398.1 eV), pyridone *N* (400.5 eV) and *N*-oxides (402–405 eV) [33]. From Fig. 4b, the dominant *N*-containing group was pyridinic and pyridone groups which are suitable for CO_2 adsorption due to the preferred interaction between the groups and CO_2. Other *N*-doped samples contained the same *N*-containing groups yet with different ratios (Fig. S3). But, the amount of nitrogen on the porous carbon's surface was increased following the amount of *N* precursor (Table 1). 1 N-KL and 2 N-KL have low nitrogen contents that are under 1.0 wt%. 4 N-KL and 8 N-KL have a higher nitrogen percentage of 1.10, and 1.17 wt%, respectively.

3.2 CO_2 adsorption behavior

The CO_2 adsorption isotherm of 1 N-KL to 8 N-KL, and KL700 at 298 K up to 10 atm is shown in Fig. 5a and Table 2. The finest adsorbent for CO_2 adsorption was 4 N-KL with 13.6 mmol/g, and 2 N-KL which adsorbed 13.0 mmol/g was the following one. The adsorption amount did not directly correspond to the specific surface area. KL700 with 3172 m^2/g had a larger SSA than 4 N-KL with 3021 m^2/g, but the adsorption amount of KL700 with 12.4 mmol/g was less than 4 N-KL with 13.6 mmol/g. Nitrogen sites which are on the surface of the carbon materials act as the active site when CO_2 adsorbed to the adsorbent [1]. The greater the amount of urea used as *N* precursor, the more was the increase in the amount of adsorbed CO_2 versus the surface area. And, this tendency can explain the correlation between the amount of induced nitrogen and the amount of adsorbed CO_2. The amount of adsorbed CO_2 by specific surface area was 0.0039 mmol/m^2 by KL700, and it increased to 0.00404–0.0047 mmol/m^2 by 1 N-KL to 8 N-KL, respectively, at 10 atm. KL700 has the largest specific surface area (3172 m^2/g) and has no nitrogen functionality. Only with micropore volume and specific surface area, KL700 captured CO_2 2.3 mmol/g at 1 atm and 12.4 mmol/g at 10 atm. In case of 8 N-KL, too much nitrogen was loaded on the carbon's surface, and the specific surface area shrank to 2/3 than the non-doped carbon, KL700. While 8 N-KL mostly has nitrogen functionality, the CO_2 capture performance was 2.7 mmol/g at 1 atm, and 12.4 mmol/g at 10 atm, because of demolition of walls between pores and pore blocking by the abundant urea. From these results, it is certain that both porosity and nitrogen functionality would be compromised. 4 N-KL has a large surface area and adequately contains nitrogen sites.

The reversibility of CO_2 adsorption for 4 N-KL at 298 K was tested over 10 cycles up to 10 atm (Fig. 5b, c). During the ten cycles, CO_2 adsorption performance was maintained at 96–102%, almost same to the original performance. Adsorption capacities for the first cycle and tenth cycle are almost identical, with generally overlapped desorption and adsorption curves. Thus, CO_2 capture in 4 N-KL is highly reversible and primarily based on physical adsorption.

Heat of adsorption (Q_{st}), which shows the interaction between CO_2 and adsorbents was calculated by the adsorption isotherms done at 25 °C and 50 °C. The enthalpy was calculated using the Clausius–Clapeyron equation [34].

$$\Delta H^{\circ}_{ads} = R\left[\frac{\partial \ln P}{\partial (1/sT)}\right]_{\theta}$$

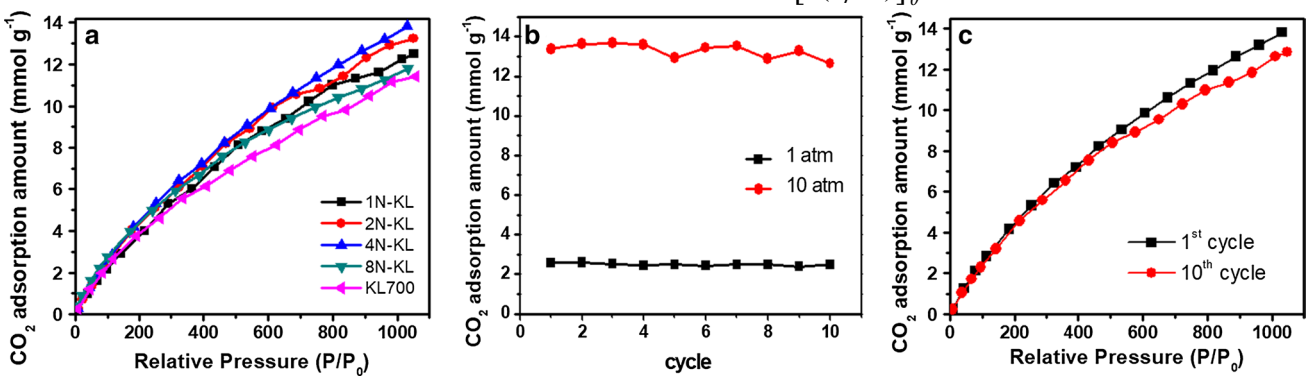

Fig. 5 **a** CO_2 adsorption amount from 0.05 to 10 atm, **b** CO_2 adsorption cycle with 4 N-KL, **c** First cycle and tenth cycle of CO_2 adsorption graph with 4 N-KL

Table 2 CO_2 uptakes of various adsorbents *x*N-KL and KL700 at 25 °C

	1 N	2 N	4 N	8 N	KL700
CO_2 adsorption at 1 atm (mmol g^{-1})	2.2	2.5	2.6	2.7	2.3
CO_2 adsorption at 10 atm (mmol g^{-1})	12.2	13.0	13.6	11.6	12.4
CO_2 adsorption amount by SSA (mmol m^{-2})	0.0040	0.0042	0.0045	0.0047	0.0039

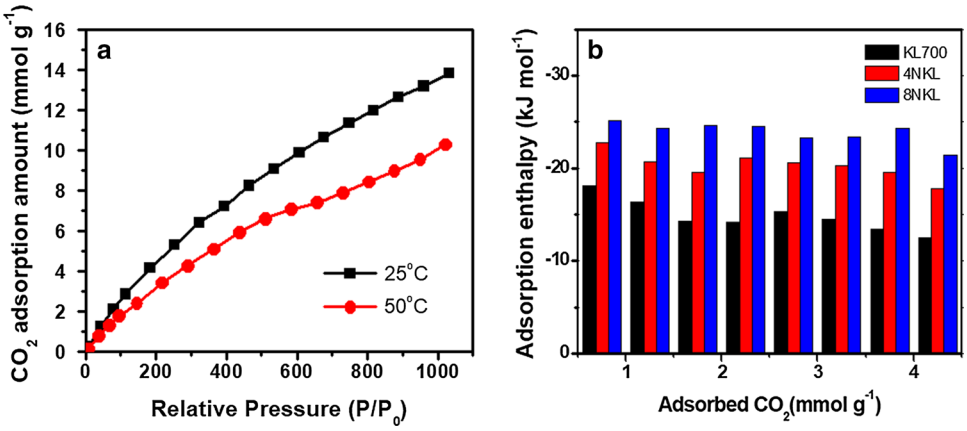

Fig. 6 **a** Adsorbed CO_2 amount with 4 N-KL versus relative pressure at 25 °C and 50 °C, **b** calculated adsorption enthalpy of KL700, 4 N-KL and 8 N-KL using the Clausius–Clapeyron equation

where ΔH°_{ads} is the heat of adsorption, and R is the ideal gas constant. A plot of $\partial \ln P$ and $\partial(1/T)$ gives a linear equation, and the gradient of the equation is proportional to adsorption heat. Figure 6 shows the curves of the calculated enthalpy at each adsorbed CO_2. The adsorption enthalpy shows physical adsorption performance, but the adsorption heat of absorbent which has more *N*-doping sites is greater than the other [35]. The average adsorption enthalpy of 8 N-KL, 4 N-KL and KL700 is − 24 kJ/mol, 21 kJ/mol and − 15 kJ/mol, respectively. If the enthalpy is higher than in KL700, it means that there is enhanced interaction between CO_2 and nitrogen-doped site of adsorbent.

4 Conclusion

In summary, the *N*-doped nanoporous carbon was developed with KOH activation and urea modification from abundant biomass lignin. Lignin-based porous carbon was synthesized with a BET surface area over 3000 m^2/g and nitrogen content over 1.0 wt%. The surface functionalities were characterized in detail by XPS, Raman, SEM, and TEM. CO_2 adsorption experiments were performed at 298 K from 1 atm to 10 atm. The final product, 4 N-KL can adsorb CO_2 more than 13 mmol/g at 10 atm which is more than adsorption capacities of other samples due to the existence of *N* content and optimized porous structure. For enthalpy calculation, adsorption tests were checked at higher temperature over 298 K. Cycle tests were performed over ten cycles from 0.05 to 10 atm and the structure and nitrogen functionality survived after the ten cycles.

Acknowledgements This research was supported by both the National Research Foundation (NRF) funded by the Ministry of Science, ICT, and Future Planning (No. 2017M2A2A6A01021187), and the Energy Technology Development Project (ETDP) funded by the Ministry of Trade, Industry, and Energy (20172410100150), Republic of Korea.

References

1. Hao GP, Li WC, Qian D, Lu AH (2010) Rapid synthesis of nitrogen-doped porous carbon monolith for CO_2 capture. Adv Mater 22:853
2. Rahman FA, Aziz MMA, Saidur R, Bakar WAWA, Hainin MR, Putrajaya R, Hassan NA (2017) Pollution to solution: Capture and sequestration of carbon dioxide (CO_2) and its utilization as a renewable energy source for a sustainable future. Renew Sustain Energy Rev 71:112
3. Seema H, Kemp KC, Le NH, Park S-W, Chandra V, Lee JW, Kim KS (2014) Highly selective CO_2 capture by S-doped microporous carbon materials. Carbon 66:320
4. Zhuo H, Hu Y, Tong X, Zhong L, Peng X, Sun R (2016) Sustainable hierarchical porous carbon aerogel from cellulose for high-performance supercapacitor and CO_2 capture. Ind Crops Prod 87:229
5. Chen C, Park D-W, Ahn W-S (2014) CO_2 capture using zeolite 13X prepared from bentonite. Appl Surf Sci 292:63
6. Verdegaal WM, Wang K, Sculley JP, Wriedt M, Zhou H-C (2016) Evaluation of metal-organic frameworks and porous polymer networks for CO_2-capture applications. Chemsuschem 9:636
7. Zhu X, Do-Thanh C-L, Murdock CR, Nelson KM, Tian C, Brown S, Mahurin SM, Jenkins DM, Hu J, Zhao B, Liu H, Dai S (2013) Efficient CO_2capture by a 3D porous polymer derived from Tröger's base. ACS Macro Lett 2:660
8. Chen J, Yang J, Hu G, Hu X, Li Z, Shen S, Radosz M, Fan M (2016) Enhanced CO_2 capture cof nitrogen-doped biomass-derived porous carbons. ACS Sustain Chem Eng 4:1439
9. Plaza MG, González AS, Pis JJ, Rubiera F, Pevida C (2014) Production of microporous biochars by single-step oxidation: effect of activation conditions on CO_2 capture. Appl Energy 114:551
10. Sethia G, Sayari A (2015) Comprehensive study of ultra-microporous nitrogen-doped activated carbon for CO_2 captur. Carbon 93:68
11. Xing W, Liu C, Zhou Z, Zhang L, Zhou J, Zhuo S, Yan Z, Gao H, Wang G, Qiao SZ (2012) Superior CO_2 uptake of N-doped activated carbon through hydrogen-bonding interaction. Energy Environ Sci 5:7323
12. Saha D, Van Bramer SE, Orkoulas G, Ho H-C, Chen J, Henley DK (2017) CO_2 capture in lignin-derived and nitrogen-doped hierarchical porous carbons. Carbon 121:257

13. Sevilla M, Parra JB, Fuertes AB (2013) Assessment of the role of micropore sand N-doping in CO_2 capture by porous carbons. ACS Appl Mater Interfaces 5:6360
14. González AS, Plaza MG, Rubiera F, Pevida C (2013) Sustainable biomass-based carbon adsorbents for post-combustion CO_2 capture. Chem Eng J 230:456
15. Huang Y-F, Chiueh P-T, Shih C-H, Lo S-L, Sun L, Zhong Y, Qiu C (2015) Microwave pyrolysis of rice straw to produce biochar as an adsorbent for CO_2 capture. Energy 84:75
16. Ello AS, de Souza LKC, Trokourey A, Jaroniec M (2013) Coconut shell-based microporous carbons for CO_2 capture. Microporous Mesoporous Mater 180:280
17. Hao W, Björkman E, Lilliestråle M, Hedin N (2013) Activated carbons prepared from hydrothermally carbonized waste biomass used as adsorbents for CO_2. Appl Energy 112:526
18. Bae J-S, Su S (2013) Macadamia nut shell-derived carbon composites for post combustion CO_2 capture. Int J Greenh Gas Control 19:174
19. Zhu B, Shang C, Guo Z (2016) Naturally nitrogen and calcium-doped nanoporous carbon from pine cone with superior CO_2 capture capacities. ACS Sustain Chem Eng 4:1050
20. Kan T, Strezov V, Evans TJ (2016) Lignocellulosic biomass pyrolysis: a review of product properties and effects of pyrolysis parameters. Renew Sustain Energy Rev 57:1126
21. Funke A, Ziegler F (2010) Hydrothermal carbonization of biomass: A summary and discussion of chemical mechanisms for process engineering. Biofuels Bioprod Biorefin 4:160
22. Lucian M, Fiori L (2017) Hydrothermal carbonization of waste biomass: process design, modeling, energy and cost analysis. Energies 10:211
23. Wang J, Kaskel S (2012) KOH activation of carbon-based materials for energy storage. J Mater Chem 22:23710
24. Sun F, Gao J, Liu X, Pi X, Yang Y, Wu S (2016) Porous carbon with a large surface area and an ultrahigh carbon purity via templating carbonization coupling with KOH activation as excellent supercapacitor electrode materials. Appl Surf Sci 387:857
25. Yu H, Roller JM, Mustain WE, Maric R (2015) Influence of the ionomer/carbon ratio for low-Pt loading catalyst layer prepared by reactive spray deposition technology. J Power Sources 283:84
26. Etacheri V, Wang C, O'Connell MJ, Chan CK, Pol VG (2015) Porous carbon sphere anodes for enhanced lithium-ion storage. J Mater Chem A 3:9861
27. Choi MS, Park S, Lee H, Park HS (2018) Hierarchically nanoporous carbons derived from empty fruit bunches for high performance supercapacitors. Carbon Lett 25:103
28. Li B, Dai F, Xiao Q, Yang L, Shen J, Zhang C, Cai M (2016) Nitrogen-doped activated carbon for a high energy hybrid supercapacitor. Energy Environ Sci 9:102
29. Ma X, Cao M, Hu C (2013) Bifunctional HNO_3 catalytic synthesis of N-doped porous carbons for CO_2 capture. J Mater Chem A 1:913
30. Li Y, Wang G, Wei T, Fan Z, Yan P (2016) Nitrogen and sulfur co-doped porous carbon nanosheets derived from willow catkin for supercapacitors. Nano Energy 19:165
31. Wu Z-S, Parvez K, Winter A, Vieker H, Liu X, Han S, Turchanin A, Feng X, Müllen K (2014) Layer-by-Layer assembled heteroatom-doped graphene films with ultrahigh volumetric capacitance and rate capability for micro-supercapacitors. Adv Mater 26:4552
32. Zhang LL, Zhao X, Stoller MD, Zhu Y, Ji H, Murali S, Wu Y, Perales S, Clevenger B, Ruoff RS (2012) Highly conductive and porous activated reduced graphene oxide films for high-power supercapacitors. Nano Lett 12:1806
33. Lim G, Lee KB, Ham HC (2016) Effect of N-containing functional groups on CO_2 adsorption of carbonaceous materials: a density functional theory approach. J Phys Chem C 120:8087
34. Chen C, Ahn W-S (2011) CO_2 capture using mesoporous alumina prepared by a sol–gel process. Chem Eng J 166:646
35. Zhang S, Li Z, Ueno K, Tatara R, Dokko K, Watanabe M (2015) One-step, template-free synthesis of highly porous nitrogen/sulfur-codoped carbons from a single protic salt and their application to CO_2 capture. J Mater Chem A 3:17849